metals

MDPI

Article

The Importance of Mixing Time in Intensely Stirred Metallurgical Reactors: Applied on Decarburization Reactions

Serg Chanouian *, Henrik Larsson and Mikael Ersson

Material Science Department, KTH-Royal Institute of Technology, Brinellvagen 23, 100 44 Stockholm, Sweden; hlarsso@kth.se (H.L.); bergsman@kth.se (M.E.)

* Correspondence: sergc@kth.se

Abstract: In metallurgical converter processes, numerical modeling is a useful tool for understanding the complexity of the systems. In this paper, we present a practical model that couples fluid dynamics and chemical reactions to explore the impact of mixing time on decarburization. Using computational fluid dynamics (CFD), in this study, we investigate an arbitrary metallurgical reactor with continuous oxygen supply, focusing on the Fe–C–O system. The model employs local equilibrium, a turbulence limiter, and finite volume method for mass, momentum, and energy transfer. Tracer injection points in the gas plume's rising region exhibit faster mixing, and a comparison of reaction cases reveals distinct decarburization rates based on oxygen injection distribution and the influence of turbulence on reactions. Overall, while mixing time matters, the results show that this system is primarily governed by thermodynamics and oxygen supply, and a 270% increase in mixing time increase had a small impact on the end carbon content.

Keywords: mixing time; decarburization; metallurgical processes; computational fluid dynamics

Citation: Chanouian, S.; Larsson, H.; Ersson, M. The Importance of Mixing Time in Intensely Stirred Metallurgical Reactors: Applied on Decarburization Reactions. *Metals* **2023**, *13*, 1694. https://doi.org/10.3390/met13101694

Academic Editors: Rodolfo Morales and Hong Yong Sohn

Received: 27 August 2023
Revised: 22 September 2023
Accepted: 3 October 2023
Published: 5 October 2023

1. Introduction

In intensely stirred metallurgical converter processes such as the argon oxygen decarburization process (AOD), it is common to use physical and numerical modeling as a tool for adding transparency and understanding the otherwise opaque and complex systems. A proper model could be rewarding in terms of knowledge, safety, and cost reduction for converter development. In general, metallurgical converters utilize gas blowing for decarburization. For instance, in the AOD converter, a mixture of oxygen and inert gas is typically introduced through side nozzles to decarburize the steel. The oxygen reacts with carbon in the steel and produces mainly CO. This reaction is driven by the low partial pressure of CO; hence, a mixture of oxygen with inert gas. The reaction also benefits through kinetics which is the transportation of carbon in the steel to the reaction zone. This is accomplished by the stirring that is introduced by blowing gas into the vessel. Thus, the main numerical modeling challenges are fluid transport and high temperature chemical reactions. CFD is a popular choice for modeling fluid mass transport [1–9], see Table 1. Zhu et al. [2] presented an early side-blowing model by implementing a plume model to predict mixing and turbulence behavior in 3D. The mixing time was evaluated using a tracer added at five positions, revealing that the mixing time remained largely unaffected. Notably, these positions were situated at the surface of the bath within an area corresponding to half the bath diameter, effectively placing all tracer positions near the center of the bath. Oscillation studies of a 120-ton AOD converter were carried out in refs. [3–5] with a down-scaled physical model and industrial scale numerical model. By altering the blowing rate and fill level, the researchers observed variations in the mixing times. They found that higher blowing rates led to shorter mixing times, and the mixing time initially increased and then remained constant with increasing fill levels. An optimal fill level range of 0.7 < height/diameter < 0.75 was identified. A comparison between the traditional impulse injection method

and the continuous injection method of a food coloring tracer demonstrated a remarkable reduction in mixing time variations with a continuous injection [4]. This study reported a range of approximately 20–60 s for impulse injection, whereas continuous injection yielded a narrower range of 11–24 s. Also, Visuri et al. [7] reported mixing times in the range of 7–26 s in a physical water model of an AOD with pulse tracer injection. In addition, they found an increase in mixing time when the tracer was injected at lower depths compared to near the bath surface. However, a separate numerical model study [9] that investigated an AOD converter of the same size reported a mixing time range of 100–116 s with six nozzles and 60–120 s with seven nozzles. It is important to note that these results were not validated against any industry or water model data. Tilliander et al. [6] employed a model of an AOD converter encompassing liquid, slag, and gas phases to investigate flow characteristics. The findings revealed that lower gas flow rates induced a clockwise circulation of the steel bath, with the vortex located in the upper region of the converter. Remarkably, this flow pattern aligned with the observations reported by other side-blowing models [2–5,8,9]. However, higher flow rates exhibited a more localized counterclockwise circulation behind and below the gas plume. The penetration length of the increased gas flow rate surpassed the midpoint of the domain, reaching close to the wall opposite to the nozzles. Interestingly, these findings contradict the observations in Refs. [3,9], where the horizontal gas jet penetration did not exceed past the vessel's midpoint.

Table 1. Previous fluid dynamic models on intensive metallurgical converters that utilize gas blowing.

Ref.	Year	Pro	Sys	Inj	M	TM	MM	t_{miz}	React	Note	First Author
[2]	1998	AOD	WM	b, s + t	N	$k\epsilon$	n/a	x	n/a	Plume	Zhu
[3]	2010	AOD	WM/120 ton	s	P + N	R$k\epsilon$/SST-SAS	VOF + DPM	x	n/a	Oscillation	Odenthal
[4]	2012	AOD	WM/120 ton	s	P	n/a	n/a	x	n/a	Mixing	Wuppermann
[5]	2013	AOD	WM/120 ton	s	P + N	SST-SAS	VOF + DPM	n/a	n/a	Oscillation	Wuppermann
[6]	2014	AOD	95 ton	s	N	$k\epsilon$	n/a	n/a	n/a	Flow	Tilliander
[7]	2016	AOD	VM/150 ton	S	P	n/a	n/a	x	n/a	Mixing	Visuri
[8]	2020	AOD	120 ton	s	N	n/a	VOF + DPM	n/a	n/a	Mass transfer	Wimmer
[9]	2023	AOD	120 ton	s	N	$k\epsilon$	EE	x	n/a	Nozzle configuration	Cheng
Current	2023	AOD	WM/1.1 ton	s	N	R$k\epsilon$	EE	x	x	High temperature reactions	Chanouian

Pro, process; Sys, system; WM, water model; Inj, injection method; b, bottom; s, side; t, top; M, model; N, numerical; P, physical; t_{miz}, mixing time; MM, multiphase model; TM, turbulence model; R, realizable; SST-SAS, shear stress transport-scale adaptive simulation; React, chemical reactions.

In general, the above-mentioned studies collectively contribute to our understanding of mixing and flow dynamics in gas-stirring converters such as the AOD converter, highlighting the importance of various parameters such as fill level, injection methods, nozzle configuration, and gas flow rates. By comprehending these factors, researchers and engineers can strive to optimize converter designs and operating conditions for improved efficiency and performance.

Although it is emphasized that mixing and flow characteristics play an important role in the metallurgical converters, the optimization of metallurgical processes, such as the AOD converter, extends beyond fluid dynamics alone. The numerical development has also considered chemical reactions, where a lot of work has been dedicated to developing reaction models [10–25], involving decarburization of the steel, see Table 2.

Table 2. Previous kinetic and chemical reaction models.

Ref.	Year	Pro	SE	DB	Ph	Met	Kinetics	SP	CFD	t_{mix}	Note	First Author
[10,11]	2002	AOD	Std, Mn, Si	Lit	g, l_{sm}, s	OABS	Mass transfer of carbon in steel	SH	n/a	n/a	Melt analysis, OD, CRE	Wei & Zhu
[12–14]	2007 2011	AOD	Std, Mn, Si	Lit	g, l_{sm}, s	OABS	Mass transfer of carbon in steel	SH	n/a	n/a	Combined top and side blowing	Zhu, Shi, Wei
[15]	2008	BOF	Fe, C, O, SI	TC	g, l_{sm}, s	GFEM	CFD	HV	x	n/a	Top blowing	Ersson
[16]	2010	AOD	Std, Mn, Si, N	HSC, Lit	g, l_{sm}, s	LAMB	Conservation eq	HV	n/a	n/a	Decarburization in bubble	Järvinen
[17–19]	2011 2016	AOD	Std, Mn, Si, N, Ni	HSC, Lit	g, l_{sm}, s	LAMB	Conservation eq	HV	n/a	n/a	Melt analysis in AOD	Järvinen & Sauli
[20]	2011	RH	Fe, C, O	FS	g, l_{sm}, s	GFEM	EERZ	ZV	n/a	n/a	Decarburization in RH	Van Ende
[21,22]	2013	AOD	Std, Ni	TC + TA2	g, l_{sm}, s	CV + GFEM	CFD	HV	n/a	n/a	LMV, CRE	Andersson
[23]	2016	LF	Std + 16	FS	g, l_{sm}, s, i	GFEM	EERZ	ZV	n/a	n/a	Kinetic LF model	Van Ende
[24]	2020	LF	Fe, Mn, Si, O + 3	TC	g, l_{sm}, s, i	GFEM	EERZ	ZV	n/a	n/a	Kinetic LF model	Mason
[25]	2022	AOD	Std + 10	TC	g, l_{sm}, s, l_{sl}	GFEM	n/a	SH	n/a	n/a	Nitrogen in AOD	Wei, W.J
Current	2023	AOD	Fe, C, O	TC	g, l_{sm}, s, l_{sl}	CV + GFEM	CFD	HV	x	x	Mixing effect on Decarburization	Chanouian

Pro, process; RH, Rustahl Heraeus; LF, lade furnace; SE, system elements; Std (standard), Fe-Cr-Co; DB, database; Lit, Literature; HSC, HSC chemistry software; FS, FactSage; TC, Thermo-Calc; TA2, TimeAOD2; Ph, phases; g, gas; l_{sm}, liquid metal; l_{sl}, liquid slag; s, slag; i, inclusions; Met, method; OABS, oxygen affinity based selectivity; LAMB, law of mass action based; GFEM, Gibbs free energy minimization; CV, control volume; SP, system pressure; SH, static homogeneous; HV, hydrostatic variation; ZV, zone variation; t_{mix}, mixing time; OD, oxygen distribution; CRE, carbon removal efficiency; LMV, local melt variations.

The critical carbon content and oxygen distribution in an AOD converter were investigated using a numerical kinetic reaction model [10,11]. Oxygen is distributed to different components in the steel based on the relative affinity of their reactions. The work suggests that in the early stages of decarburization, when the carbon levels are high, the incoming oxygen is rapidly consumed. As a result, it is controlled by the supply of oxygen. At low carbon levels, the decarburization rate is predominantly influenced by the mass transfer of carbon from the molten steel bulk to the reaction interface. Additionally, a refined version of the model has been developed to study decarburization in a combined top- and side-blowing converter, which was benchmarked against industrial heats under oxidizing and reducing conditions [12–14].

Another notable study, by Wei et al., focused on the development and testing of an AOD model capable of predicting the dissolved nitrogen content and other metal/slag compositions [25]. This model utilized thermodynamic equilibrium calculations using commercial software with reliable databases and was successfully applied to process data from 12 production-scale heats. It effectively predicted changes in dissolved nitrogen content throughout the entire AOD process, considering multiple phases such as liquid metal, liquid slag, solid slag, and gas. However, certain areas require further attention such as the implementation of different total gas pressures for nitrogen and carbon reactions, and incorporating kinetic mechanisms into the model. One drawback of the above-mentioned models is their treatment of pressure as static and homogeneous, which is particularly limiting in one-cell calculations. However, these calculations have proven to be fast and efficient for process control purposes. To overcome the limitations associated with a static pressure, Järvinen et al. addressed conservation equations in their kinetic and chemical

reaction model of the AOD process [16–19]. They developed a rate expression based on the modified law of mass action, initially studying the model on a stagnant bubble and later expanding it to a full AOD converter with locally varying conditions of a rising gas plume. This method was further enhanced to include multiple parallel reversible reactions controlled by mass transfer.

An alternative approach that differentiates itself from the reaction interface models mentioned above is the effective equilibrium reaction zone model (EERZ) [20,23,24]. Unlike the reaction interface models, the EERZ method assumes equilibrium of all phases located in an effective reaction zone at the interface, simplifying mass transfer equations by assuming equal mass transfer coefficients for a given solution. By considering the reaction volume at the interface, the mass transfer equations can be transformed into simple thermodynamic calculations, facilitating linkage to thermodynamic databases. However, physical descriptions of reaction mechanisms and kinetics for each zone are still required.

Ersson et al. [15] introduced a CFD model coupled with chemical reactions in a top blown converter which was based on local control volume equilibrium after each timestep. Andersson et al. [21,22] later applied this coupling method in the AOD converter. This approach offers a significant advantage as it eliminates the need for information regarding the interfacial surface area. In this method, if an interphase exists, the entire cell is assumed to be in equilibrium. However, this approach demands significantly greater computational effort, especially when an accurate description of mass transfer to the interface is required. This is due to the necessity of resolving multiphase features in the computational cells which further amplifies the computational requirements.

Overall, it has been highlighted that flow characteristics and mixing time are important contributing factors to a more effective process and decarburization rate in metallurgical reactors. Specifically, at low carbon levels, when the rate is governed by the mass transfer of carbon in the bulk to the reaction interface. However, to the best of our knowledge, no previous study has examined the influence of mixing time on the decarburization reaction. In most studies, it has been concluded that a decrease in mixing time is good. However, it is also reasonable to assume that there is a point where a decrease in mixing time would not yield any increase in the reaction rates. Therefore, the objective of this study is to develop a practical model that combines fluid dynamics with chemical reactions, building upon our previous work [26,27]. An arbitrary metallurgical side-blowing reactor with continuous oxygen supply is utilized in this study to investigate the aforementioned effect focusing on the decarburization reaction in a Fe–C–O system.

2. Materials and Methods

The numerical model was based on a side-blowing physical water model conducted in ref. [26]. The physical water model was used as validation for the mixing time and flow structure of the system. Subsequently, a thermodynamic database and chemical reactions were integrated into the numerical model to investigate the impact that mixing time had on decarburization. The immersion of a fast-moving jet into the liquid puts a severe limitation on the overall timestep. This is due to the very high courant numbers owing to a combination of high velocities, sharp gas–liquid interfaces, and small cells needed in the jet region. Thus, simulating high-velocity gas–liquid injections require substantial computational power. This is commonly addressed through a numerical technique [3,5,28,29], where the characteristics of the jet flow are separately simulated and then imported into the vessel in another simulation. To account for the expected significant increase in simulation time when employing a combined model that incorporates heat transfer and reactions, a decision was made to utilize a coarse model for incompressible fluid flow transportation. The injection of gas into the system was introduced further away from the wall, representing the point where the gas plume is mainly controlled by the buoyancy, i.e., after the jet penetration depth is reached. By employing this approach, it becomes feasible to capture the flow structure and mixing within the bath caused by the jet, without the necessity of simulating the high velocity and small length scales at the nozzle

outlet. With an emphasis on the practical approach, it was assumed that this would be sufficient to study decarburization in systems of industrial significance.

2.1. General Equations

The Eulerian multiphase [30] model was employed to solve the conservation of mass and momentum for each phase under a shared pressure according to Equations (1) and (2), respectively. The momentum transfer between the phases is modeled with a drag term where a diameter is specified for the secondary phase:

$$\frac{\partial}{\partial t}(\alpha_q \rho_q) + \nabla \cdot \left(\alpha_q \rho_q \vec{v}_q\right) = \sum_{p=1}^{n} (\dot{m}_{rq} - \dot{m}_{qr}) qp + S_q \tag{1}$$

where the phases are denoted as q and r, α is the volume fraction of the phase, ρ is the density, $\vec{v}$ is the phase velocity, and $\dot{m}_{rq}/\dot{m}_{qr}$ are the mass transfer from one phase to the other. The last term S_q is a source term which by default is zero.

$$\begin{aligned} \tfrac{\partial}{\partial t}\left(\alpha_q \rho_q \vec{v}_q\right) + \nabla \quad & \cdot \left(\alpha_q \rho_q \vec{v}_q \vec{v}_q\right) \\ & = -\alpha_q \nabla p + \nabla \cdot \bar{\bar{\tau}}_q + \alpha_q \rho_q \vec{g} \\ & + \sum_{p=1}^{n} \left(K_{rq}\left(\vec{v}_r - \vec{v}_q\right) + \dot{m}_{rq} \vec{v}_{rq} - \dot{m}_{qr} \vec{v}_{qr}\right) + \left(\vec{F}_q + \vec{F}_{lift,q}\right. \\ & \left. + \vec{F}_{wl,q} + \vec{F}_{vm,q} + \vec{F}_{td,q}\right) \end{aligned} \tag{2}$$

Here, p is the pressure shared by the phases, $\bar{\bar{\tau}}$ is the stress strain tensor as seen in Equation (3), and the gravitational acceleration is denoted as $\vec{g}$. K_{rq} is the interphase momentum exchange coefficient defined in Equation (4), and $\vec{v}_{rq}/\vec{v}_{qr}$ are interphase velocity. The last terms are $\vec{F}_q$ external body force, $\vec{F}_{lift,q}$ lift force, $\vec{F}_{wl,q}$ wall lubrication force, $\vec{F}_{vm,q}$ virtual mass force, and $\vec{F}_{td,q}$ turbulent dispersion force acting between the different phases.

$$\bar{\bar{\tau}}_q = \alpha_q \mu_{eff,q}\left(\nabla \vec{v}_q + \nabla \vec{v}_q^{\,T}\right) \tag{3}$$

Here, $\mu_{eff,q}$ is the effective viscosity for phase q.

$$K_{rq} = \frac{\rho_r f}{6\tau_p} d_{b,r} A_i \tag{4}$$

Here, f is the drag function defined in Equation (5) according to the Schiller–Naumann model [31], τ_r is the particulate relaxation time, $d_{b,r}$ the diameter of bubbles of phase r, and A_i is the interfacial area.

$$f = \frac{C_D Re}{24} \tag{5}$$

Here, C_D is the drag coefficient defined in Equation (6) and Re is the Reynolds number:

$$C_D = \begin{cases} \frac{24\left(1+0.15Re^{0.687}\right)}{Re}, & Re \leq 1000 \\ 0.44, & Re \geq 1000 \end{cases} \tag{6}$$

Here, the relative Reynolds number is described in Equation (7):

$$Re = \frac{\rho_q |\vec{v}_r - \vec{v}_q| d_{b,r}}{\mu_q} \tag{7}$$

where, μ_q is the viscosity for phase q.

Many types of engineering problems targeted at the metallurgical industry describe turbulence with two equations for effective viscosity approximation such as the k-ε or k-ω models (Table 1), as they have become the industry standard. While it has been demonstrated in the literature [28,29] that higher accuracy can be attained through the utilization of more sophisticated turbulence models, it is to be acknowledged that this advantage is accompanied by an increase in computational time. With an emphasis to developing a practical model, it was decided to treat the turbulence in the domain with the k-ε realizable model [32], where Equation (8) expresses the turbulent viscosity in relation to the kinetic energy (k) and turbulent dissipation rate (ε) of phase q. Here, the viscosity coefficient C_μ is a function of local flow parameters. Furthermore, Equations (9) and (10) present the modeled transport equations for k and ε, respectively:

$$\mu_t = \rho_q C_\mu \frac{k^2}{\varepsilon} \tag{8}$$

$$\begin{aligned} \frac{\partial(\alpha_q \rho_q k_q)}{\partial t} + \nabla \cdot & \left(\alpha_q \rho_q \vec{v}_q k_q\right) \\ & = \nabla \cdot \left(\alpha_q \left(\mu_q + \frac{\mu_{t,q}}{\sigma_k}\right) \nabla k_q\right) + \alpha_q (G_{k,q} + G_b) - \alpha_q \rho_q \varepsilon_q \end{aligned} \tag{9}$$

$$\begin{aligned} \frac{\partial(\alpha_q \rho_q \varepsilon_q)}{\partial t} + \nabla \cdot & \left(\alpha_q \rho_q \vec{v}_q \varepsilon_q\right) \\ & = \nabla \cdot \left(\alpha_q \left(\mu_q + \frac{\mu_{t,q}}{\sigma_\varepsilon}\right) \nabla \varepsilon_q\right) + \alpha_q \rho_q C_1 - \rho_q C_2 \frac{\varepsilon^2}{k + \sqrt{\nu \varepsilon}} \\ & + \alpha_q C_{1\varepsilon} \frac{\varepsilon}{k} C_{3\varepsilon} G_b \end{aligned} \tag{10}$$

In this context, G_k represents the production of turbulent kinetic energy resulting from velocity gradient, while G_b signifies the production of turbulent kinetic energy due to buoyancy. The turbulent Prandtl numbers for k and ε are denoted as σ_k and σ_ε, respectively, and ν represents the kinematic viscosity. $C_{1\varepsilon}$ and C_2 are constants while $C_{3\varepsilon}$ is a coefficient which determines the influence of buoyancy on ε, and C_1 is expressed as Equation (11):

$$C_1 = \max[0.43, \frac{\eta}{\eta + 5}], \ \eta = S\frac{k}{\varepsilon}, \ \ S = \sqrt{2 S_{ij} S_{ij}} \tag{11}$$

Based on the first law of thermodynamics, the energy equation is expressed in Equation (12):

$$\frac{\partial}{\partial t}(\alpha_q \rho_q h_q) + \nabla \cdot \left(\alpha_q \rho_q \vec{v} h_q\right) = \alpha_q \frac{\partial p_q}{\partial t} + \nabla \cdot \left[\left(k_{eff} \nabla T\right) - \left(\bar{\bar{\tau}}_{eff} \cdot \vec{v}\right)\right] + S_h \tag{12}$$

The specific enthalpy h_q is presented in Equation (13), k_{eff} is the effective thermal conductivity, $\bar{\bar{\tau}}_{eff}$ is the shear energy, and S_h is a source term.

$$h = e + \frac{p}{\rho} \tag{13}$$

where, e is the specific internal energy.

2.2. Boundary Conditions and Setup

The geometry was designed based on the water model in ref. [26], as shown in Figure 1, where gas injection occurs through two cell zones as a mass source, according to Equation (14) [30]. This represented the two side injections in the physical model, where the axial momentum of the jet is almost completely dissipated, and buoyancy drives the jet in the vertical direction. The volumes were positioned at some distance from the jet inlet, having their horizontal endpoint aligned with the average penetration depth measured in the physical model. This assumption was based on observations of the physical model,

Figure 2. The buoyant plume region starts at some distance from the wall and ends at, approximately, the jet penetration depth.

$$\frac{\dot{m}}{V} \tag{14}$$

where, $\dot{m}$ is the mass flow rate and V is the volume of the cell zone.

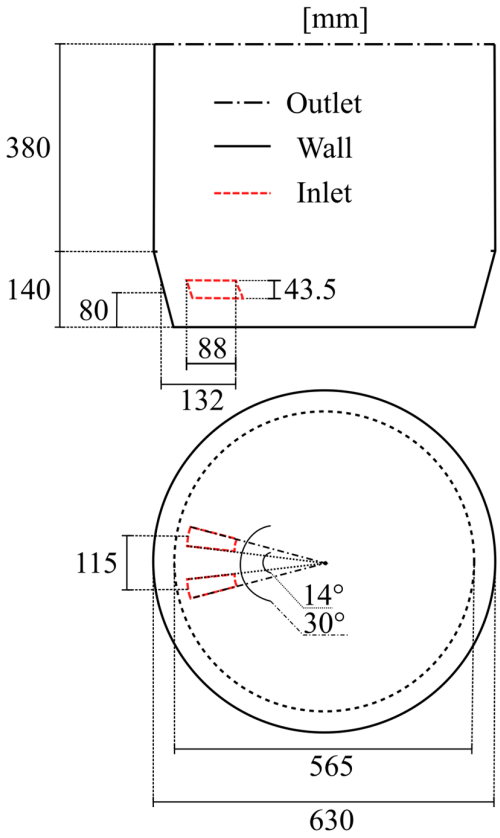

Figure 1. Schematic illustration of numerical geometry, side and top views.

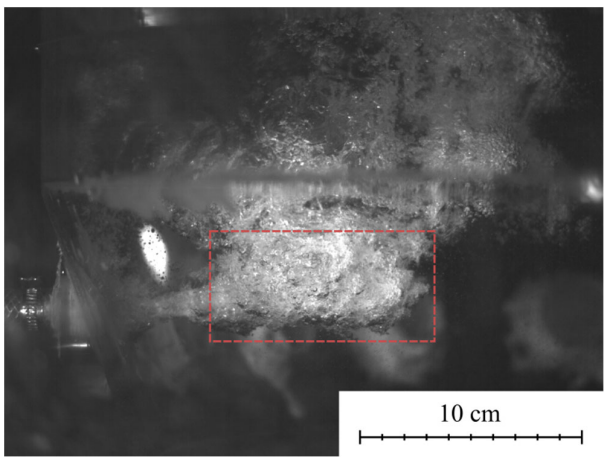

Figure 2. Image capturing the penetration depth of the physical water model. The red-dashed box represents the injection zone utilized in the numerical model.

A flat surface approach was used with degassing as boundary conditions and the walls were set to non-slip. The phase coupled SIMPLE algorithm (semi-implicit method for pressure-linked equations) was employed to solve the pressure velocity coupling, and the

spatial discretization utilized the second-order upwind for momentum, pressure, and first order turbulence, and user-defined scalars (UDS), with first-order implicit time integration. The key parameters for the system are presented in Table 3.

Table 3. Key parameters of the WM simulation.

Parameter	Nomenclature	Water (*l*)	Gas (*g*)
Density	ρ (kg·m^{-3})	998	1.3
Dynamic viscosity	μ (kg·m^{-1}·s^{-1})	1.0×10^{-3}	1.8×10^{-5}
Mass flow rate per inlet	$\dot{m}$ (kg·s^{-1})	-	0.0052
Bubble diameter	d_b (m)	-	0.01
Degassing pressure	p (Pa)	101,325	101,325

2.3. Fluent and Thermo-Calc Coupling Scheme

The model coupled ANSYS Fluent v2022 R2 [30] with Thermo-Calc v2021b [33] ("TC" from now on). This is achieved using the C programming language, with the aid of the application programming interfaces (API) present in ANSYS Fluent and TC. The API in Fluent is the user-defined function (UDF) and the API in TC is called TQ. The model uses Fluent for the heat and mass transfer in the domain and TC for the high temperature reactions. The TCS metal oxide solutions (TCOX10) [34] database was used for the current setup. TCOX is a thermodynamic database designed for slags and oxides, enabling the description of solid slag, liquid steel, and slag as phases with varying compositions separated by a miscibility gap. These phases are referred to as ionic liquids, where, e.g., ionic liquid #1 represents liquid metal and ionic liquid #2 represents liquid slag, facilitating a continuous transition in composition from metallic to oxidic states in equilibrium. Thermo-Calc typically employs the minimization of Gibbs free energy method to compute multi-component phase equilibria, accommodating different phases such as gas, liquid, and slag. For the purpose of this study, the system was limited to the elements C, Fe, and O, thereby reducing computational time in TC by minimizing the number of chemical reactions and including the ones relevant to the decarburization process.

The process of solving for heat and mass transfer combined with high temperature reactions is described as follows: First, an assumption is made that there is a one-way coupling between the flow and the reactions, meaning that the reactions do not affect the flow pattern (velocity field). This means that an incompressible solver with a frozen flow field approximation can be used. At the end of each timestep, before calling TC, the pressure, temperature, and composition of elements are collected in cells that undergo reactions. These data are passed from Fluent to TC. The enthalpy of each phase is calculated separately using TC. Since it is likely that each phase is in a non-equilibrium state, a final equilibrium calculation is performed with all phases and the total enthalpy as equilibrium conditions to find the temperature and new phase compositions of the cell.

In this way, the composition per phase and temperature changes locally in the cell at the end of the timestep, and the mass transfer handles the macro kinetics, i.e., the transport of mass in and out of the reaction zone at the next timestep, Figure 3. Even though the values are updated directly at the end of each timestep, a reaction rate is needed for each cell. In the current work, this is introduced through a turbulence dependent reaction rate that sets a limit on how much of the cell mass can reach equilibrium during a timestep, which is discussed in the case section below. When addressing reactive multiphase flows, the preservation of mass is crucial. In the present work, the approach taken ensures that in TC, while heat and work may be exchanged across the system boundaries, the total mass and atoms of the system remains constant (control mass). In contrast, Fluent adopts an open system (control volume) approach, enabling the transfer of heat, work, and mass across the system boundaries, as depicted in Figure 4a. Note that each computational cell is treated as a separate system. The difference between these two approaches is that the control volume approach does not allow a change in system volume between equilibrium and

non-equilibrium states. This restriction can be handled by using two-way coupling where fluid properties and mass transfer between phases are made part of the CFD solver iterative process. However, this would increase the computational time dramatically, which is why the current model proposes a different approach. Here, constant density is used in each control volume, and the frozen flow field does not admit any changes in phase fractions in the CFD solution field. Conversely, in the control mass, the density and the phase fractions are allowed to vary when a new equilibrium state is calculated. Thus, a mass conservation of the elements in phases can be obtained by scaling the element composition for each phase when the element mass is updated in the CFD solver. This admits a state where the mass of a certain phase can increase or decrease, while the density is kept constant. A scale factor that is lower than one indicates that the density (or pressure) likely would be lower for the phase in question, while a value higher than one indicates a higher density (or pressure). The density and phase fraction are kept constant so the CFD solver will not experience a change in the flow field due to the reactions (i.e., a "one-way coupling"). This is a practical approach that conserves the mass of each element while allowing the use of a fully incompressible solver. Figure 4b illustrates the concept of keeping the density constant during the reactive process.

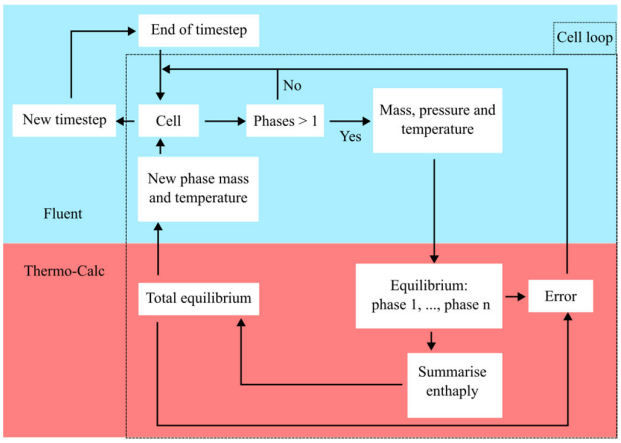

Figure 3. Flowchart of the fluid transport and chemical reactions coupling scheme.

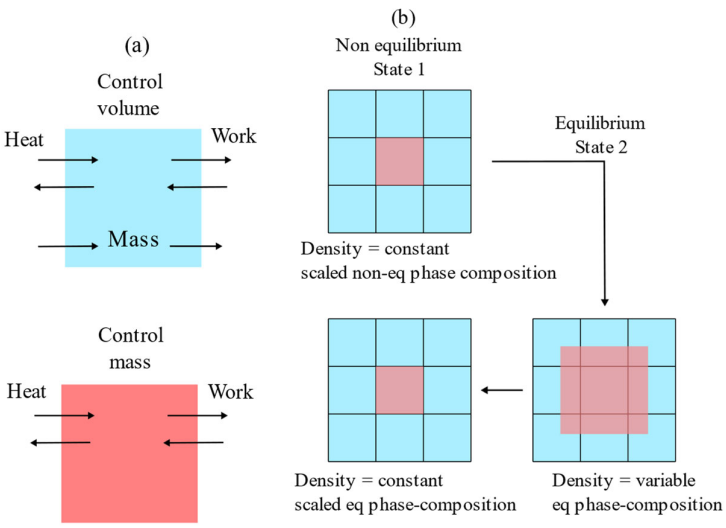

Figure 4. (**a**) Illustration of the difference between the control volume and control mass approach; (**b**) illustration of the mass conservation with constant density where total mass is conserved.

2.4. Numerical Procedure

2.4.1. Water Model

Prior to adding chemical reactions, the water model simulation was configured to progress using a transient formulation over a duration of 50 s, employing a timestep size of 0.01 s. Subsequently, a frozen flow field was adopted, and the concentration of an inert scalar was tracked to monitor the mixing time. To examine if the frozen flow field was at a quasi-steady state, this process was repeated three times, with each iteration continuing with a 10 s increment in the transient flow field simulation. The mixing time was determined using a frozen flow field at specific time intervals of 50, 60, and 70 s during the transient flow.

2.4.2. Mixing Time

The mixing time represents a characteristic period dictating the duration required for a change to propagate throughout the majority of a given process. Specifically, the mixing time is defined based on a predetermined criterion that indicates the achievement of a highly homogeneous state. In this study, the criterion for determining the mixing time is set at 95% total homogenization, denoting the time necessary to reduce concentration differences to within ±5% of the mean concentration. The simulation employed a user-defined scalar (UDS) model, which solved Equation (15) [30], in order to calculate the mixing time:

$$\frac{\partial}{\partial t}\left(\alpha_q \rho_q \varnothing_q^i\right) + \nabla\cdot\left(\alpha_q \rho_q \vec{v}_q \varnothing_q^i - \alpha_q \Gamma_q^i \nabla \varnothing_q^i\right) = 0, \;\; i = 1, \ldots, N \tag{15}$$

Here, the arbitrary scalar i in phase q is represented by $\varnothing_q^i$, while Γ_q^i is the diffusion coefficient in turbulent flows determined by Equation (16):

$$\Gamma = \rho D_m + \frac{\mu_t}{SC_t} \tag{16}$$

where, the molecular mass diffusivity is D_m and SC_t is the turbulent Schmidt number (0.7) which is expressed as $\frac{\mu_t}{\rho D_t}$ with D_t being turbulent diffusivity.

Nine different tracers with the same fluid properties as the water were injected into different positions in the domain, see Figure 5, in order to observe the effect of injection position on the mixing time. The mixing time of each tracer was monitored with a volumetric method which was implemented by tracking the standard deviation of the mass-averaged tracer concentration using Equation (17):

$$\sigma_{std} = \sqrt{\frac{1}{N}\sum_{i=1}^{N}\left(\frac{x_i - x_\infty}{x_\infty} \times 100\right)^2} \tag{17}$$

Here, the number of cells is denoted as N; x_i and x_∞ are the concentration of tracer in the cell and the mean concentration, respectively.

Under the assumption of a normal distribution of tracer concentration within the domain, on the one hand, one standard deviation captures the homogenization degree (±5%) within approximately 67% of the cells. On the other hand, two standard deviations capture 95% of the cells, serving as an appropriate representation of the mixing time in this case. Thus, the mixing time was determined as the point when the relative standard deviation of the tracer in the domain dropped below 2.5%.

This mixing time was measured in 3 different butterfly-structured meshes, of sizes: 16,562 (coarse), 43,956 (medium), and 76,545 (fine) The mesh sensitivity was studied using the mixing time of all tracer injections in the fine, medium, and coarse meshes.

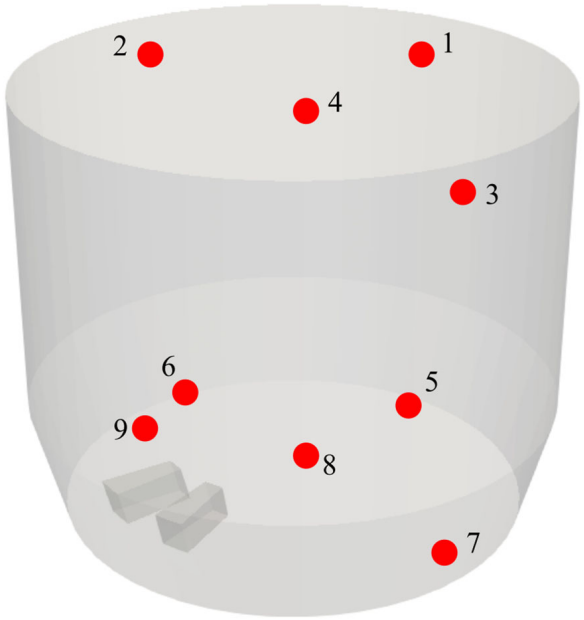

Figure 5. Figure illustrating 9 different positions of tracer injections with the red dots.

2.4.3. Theoretical Model Cases

A metal reactor model was developed using the medium mesh of the water model. In this setup, the model was modified to simulate the physical properties of liquid steel. The objective of this model was to obtain a solution for decarburization in a hypothetical metal reactor, where the energy equation was solved as well as accounting for chemical reactions. The key system parameters can be found in Table 4.

Table 4. Key parameters of metal reactor simulation.

Parameter	Nomenclature	Liquid Steel (*l*)	Gas (*g*)
Density	ρ (kg·m^{-3}]	7000	1.3
Dynamic viscosity	μ (kg·m^{-1}·s^{-1})	6.3×10^{-3}	1.8×10^{-5}
Mass flow rate per inlet	$\dot{m}$ (kg·s^{-1})	-	0.0052
Bubble diameter	d_b (m)	-	0.01
Degassing pressure	p (Pa)	101,325	101,325
Specific heat	C_p (J·kg^{-1}·K^{-1})	800	1006
Thermal conductivity	k_c 9W·m^{-1}·K^{-1})	64	0.0242

The measurement of mixing time was conducted following the above-mentioned procedure, wherein a fixed flow field was considered after a transient flow of 70 s, accompanied by the injection of tracers at nine distinct points. However, to account for the combined influence of advection and diffusion on the mixing process [35], two measurements were performed. In the first, an effective diffusion coefficient was applied to all tracers in accordance with Equation (16), while in the second, only a laminar diffusion coefficient was assumed by assigning a constant of 1×10^{-9} kg·m^{-1}s^{-1}. The latter assumes a negligible diffusion contribution to the mixing. This enabled an examination of the mixing impact on the chemical reactions, while maintaining consistent conditions for mass flow rate, which otherwise certainly would impact the decarburization.

Further, the coupling to TC was introduced to the frozen flow field with adiabatic boundaries and UDS to transport each element. The thermodynamic system consisted of liquid steel with C, Fe, and O in all of the below mentioned cases and with oxygen as process gas supplied into the system. The process gas assumed the steel temperature instantaneously, and the reactions took place if the gas volume fraction was between 0.1–0.9

in the computational cell. Table 5 presents the initial composition and temperature of the following cases and simulations. A workstation, equipped with two AMD EPYC 7301 processors featuring 16 cores each, and a combined RAM capacity of 128 GB, computed all cases with 10 min of real time for each case, employing a timestep of 0.1 s. Three simulations were conducted for all cases with the first (a), setting the reference, the second (b), using only a laminar mass diffusion coefficient (i.e., no turbulent diffusion) in order to artificially increase the mixing time, and the third (c), changing the initial oxygen mass fraction. All the simulations assumed that solid oxides formed during reactions would be inert after formation and would, therefore, not participate in any subsequent reactions. This assumption was made to reduce the number of transport equations to be solved due to the extremely low amounts of solid oxides forming in the current process (Figure 6).

Table 5. Initial composition and temperature of cases in conducted simulations.

Test	W (C)	W (Fe)	W (O)	Temperature (K)
a	0.001	0.9987	0.0003	1793
b	0.001	0.9987	0.0003	1793
c	0.001	0.9989	0.0001	1793

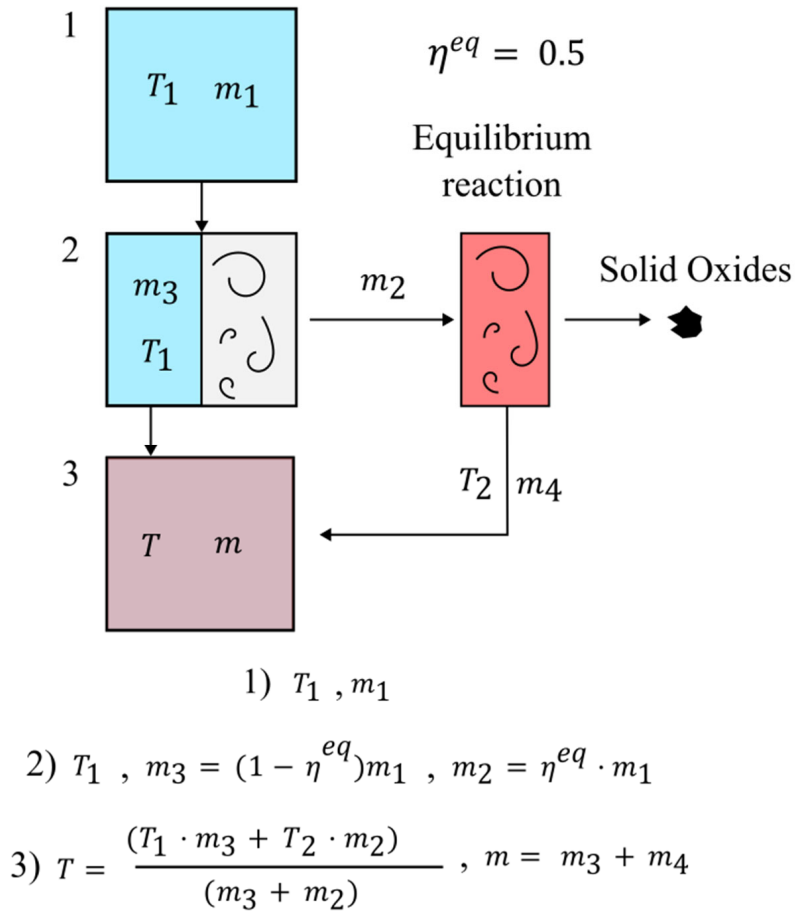

Figure 6. Schematic illustration of turbulent reaction rate treatment in coupled model, where m denotes the mass and T is the temperature in the cell.

Case 1–Simplified Oxygen Injection, No Transport of Products

The first case was created to investigate how a simplified oxygen injection model would affect the results. The equilibrium reaction frequency was set as the inverse of the gas hold-up of the plume (0.6 s). The injected oxygen was distributed equally across all

cells participating in the reactions. This assumes that the oxygen could spread across the plume region without triggering any reactions until the plume was filled with the oxygen that entered the domain during the gas holdup time. The gaseous products (mainly CO) were assumed to leave the domain within the gas holdup time. Case 1 reduces the number of equilibrium calculations at the expense of not accounting for the full transport process taking place in the plume. It should be noted that the transport of elements and energy in the liquid melt took place at the regular CFD timestep.

Case 2–Oxygen Injection in the Jet Zone, No Transport of Products

The second case looked at another extreme, namely what happens if all oxygen reacts at the injection zone. The equilibrium reaction frequency was set to the inverse of the timestep. Similar to Case 1, there was no transport of gaseous products. The main difference compared to Case 1 was the higher reaction frequency and the higher average reaction pressure due to all reactions taking place in the injection zone.

Case 3–Oxygen Injection in the Jet Zone

In the third case, the reactions were limited to the injection zone, similar to Case 2, and the equilibrium reaction frequency was set to the inverse of the timestep. However, this time, the gaseous products were transported in the domain and were allowed to react freely with the liquid melt if they were in the domain. The cost of this added complexity substantially increased the number of cells in which reactions took place during a timestep, thereby increasing the simulation time accordingly.

Case 4–Oxygen Injection in the Jet Zone, Reactions Limited by Turbulence

The fourth case is similar to Case 3. However, in the previous cases, the only limitations to the reactions were the transportation of elements in and out of the reaction zone and the oxygen rate supply. The reaction rate in Case 3 was essentially infinite, where the entire amount of gas present in a cell would react with the entire amount of liquid in that cell. In Case 4, a reaction rate limited by turbulence was introduced by applying the Eddie dissipation concept (EDC) [30,36]. The concept is based on the energy transfer from large eddies to the smallest eddies referred to as fine structures in turbulent flow. The primary generation of turbulent kinetic energy occurs through the interactions between larger eddies and the mean flow. In this process, mechanical energy is transferred from the eddy structures to the fine structures. Most of the dissipation of kinetic energy into heat happens in these fine structures due to work done by molecular forces on the turbulent eddies. The EDC model assumes that the reactions occur in the fine scales occupied by the volume fraction which can be expressed by Equation (18), and the reacting species are assumed to react over a timescale expressed as Equation (19):

$$\xi^{*\prime} = C_{\xi}\left(\left(\frac{\nu\varepsilon}{k^2}\right)^{\left(\frac{1}{4}\right)}\right)^3 \tag{18}$$

$$\tau^* = C_{\tau}\left(\frac{\nu}{\varepsilon}\right)^{\left(\frac{1}{2}\right)} \tag{19}$$

Here, C_{ξ} and C_{τ} are the volume fraction constant (2.1337) and time scale constant (0.4082), respectively.

With Equations (18) and (19), it was possible to assume an equilibrium fraction within each cell over a timestep (t_s), according to Equation (20):

$$\eta^{eq} = \xi^{*\prime} \cdot \frac{t_s}{\tau^*} \tag{20}$$

As an example, if the equilibrium fraction were 0.5 in a cell, only half of the element masses would react in TC, the new phase composition would then blend with the unreacted mass in the computational cell, as illustrated in Figure 6.

3. Results and Discussion

The decarburization reaction was modeled in a side-blowing metal reactor with fluid transport and chemical reactions. The model was rather coarse to focus on a practical approach to coupled modeling with reasonable computational time. The mixing time measurements of three grid resolutions were compared to a physical water model, presented in Figure 7. It is clear from the figure that the average mixing time is converging to a value slightly below the experimental range. All simulations reached a quasi-steady state and showed no variation in mixing time at 50, 60, and 70 s. Instead, the vertical arrows, seen in Figure 7a, represent the interval on mixing times acquired from injecting the tracer in different positions, as depicted in Figure 7b (from Figure 5). These results suggest that the location of the injection point is important when determining the mixing time, as Points 1, 4, 5, 8, and 9 clearly show a faster mixing of the tracer. These injection points are located in the trajectory of the commonly reported [2–6,8,9] large circulation which appears in side-blowing models. In such side-blowing processes, the convective contribution to the mixing is very high, as seen in Figure 8, where a large portion of the bath is affected by strong currents. Similar results were also found in experiments carried out by Visuri et al. [7]. As discussed in ref [35], mixing refers to the process of achieving homogenization in a substance that is initially heterogeneous, accomplished through either bulk motion at a macroscopic level and or molecular diffusion at a microscopic level. However, when considering molecular diffusion alone, it is often inadequate for rapidly attaining a uniform mixture due to the limited speed of the process. Additionally, the small scales involved in mixing make it impractical to generate turbulent flow, which is commonly employed in macro-scale systems to achieve rapid mixing. With this in mind, it is suggested that the position of the tracer injection be located near the reaction zone of the process being modeled when measuring mixing time, due to the convective contribution varying across the domain. Also, note that the water model only used one tracer injection point, which approximately corresponded to Point 1 in Figure 5.

Apart from using a relatively coarse mesh, there are some other limitations in the comparison against the water model. The absence of quantitative velocity measurements in the physical model restricts the possibility of conducting a detailed comparative analysis. Also, the degassing surface fails to account for the wave-like motion of the free surface, thereby influencing the flow in the upper region of the bath. The lack of this free surface movement as well as the coarse mesh likely contribute to the quasi-steady state flow field arising in the simulation. Consequently, the physical model does not achieve the same quasi-steady flow field observed in the numerical model. However, to achieve a higher level of resemblance to the physical model would require the incorporation of a free surface and a finer mesh, and possibly a more advanced turbulence model such as the large eddy simulation (LES). It is worth noting that implementing these improvements would significantly increase the computational time, as observed in the study conducted by Haas et al. [28,29], where a single simulation took several months to complete. Given the focus of this current study, i.e., to develop a practical model, it was determined that the numerical model, which successfully generated a flow field consistent with expectations for side-blowing models as well as exhibiting a reasonable mixing time, was sufficient for the next step where a coupling to chemical reactions was added.

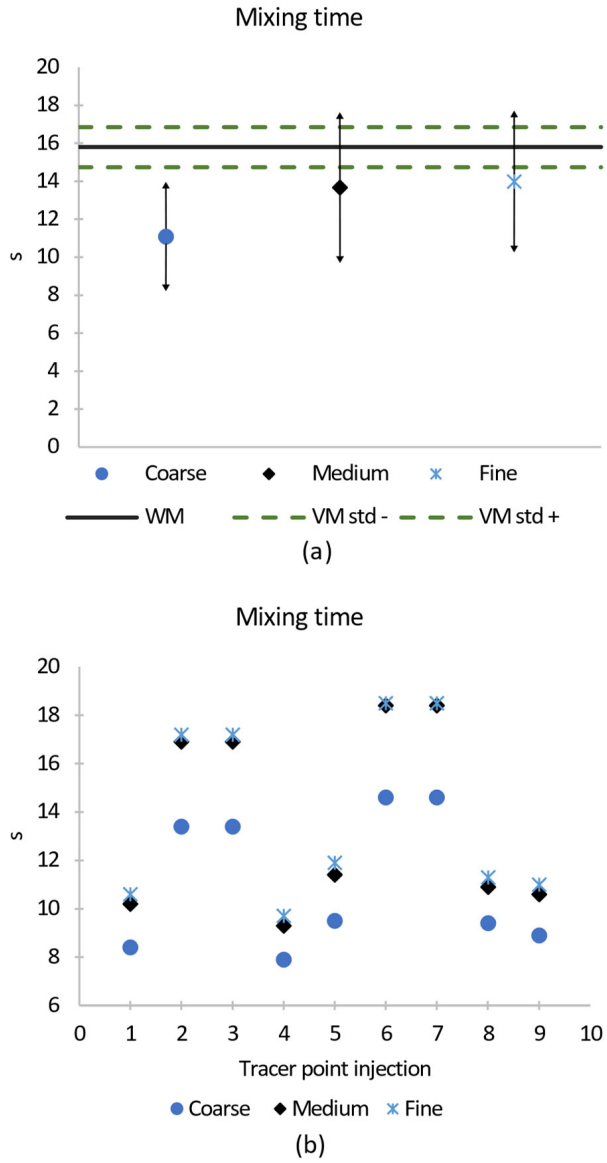

Figure 7. Mixing time comparison between the numerical model and the water model. (**a**) Shows the average value of mixing time based on all tracer injections which are displayed in (**b**).

Among the coarse, medium, and fine mesh, the error estimate, according to the maximum grid convergence index (GCI) [37], was approximately 13% for the medium mesh $\left(GCI^{32}\right)$, which was deemed acceptable for the purposes of this study. The *GCI* measured at the most important plume injection point (Point 9 in Figure 5) had a value of 7%. Thus, the medium mesh was used for all subsequent simulations. Please refer to Table 6 for the GCI values related to the mixing time at all tracer injection points.

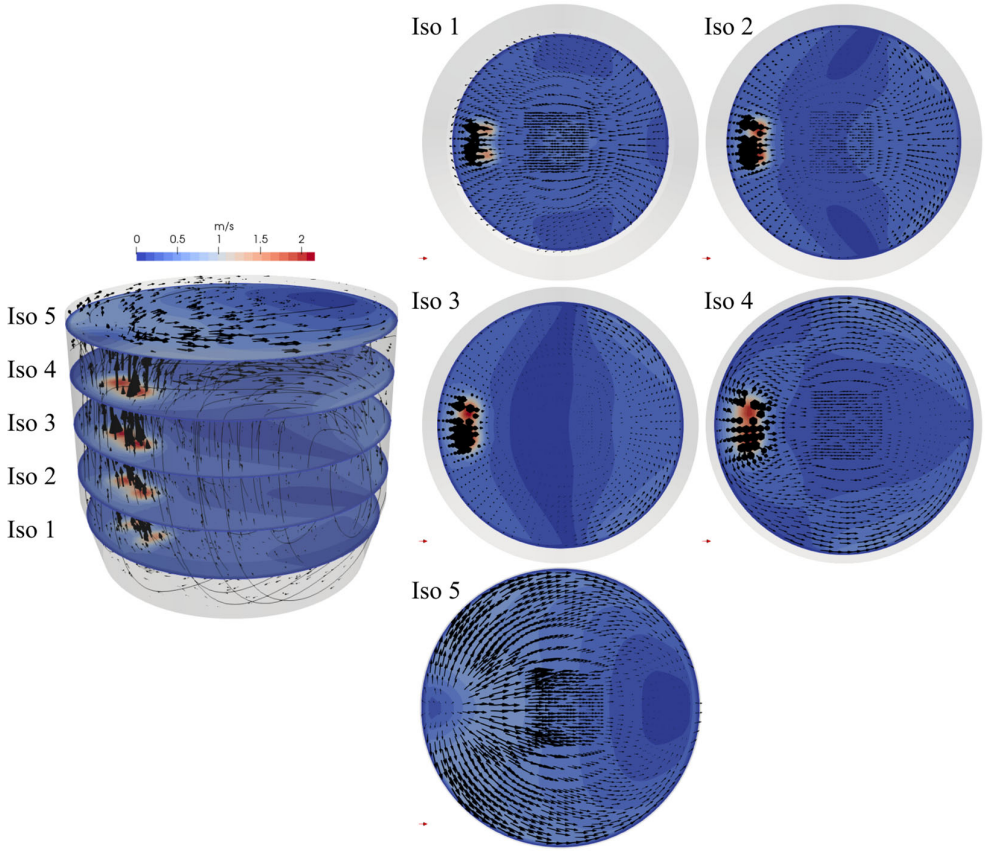

Figure 8. Displays the velocity magnitude and circular flow field caused by the rising gas in iso-planes. Velocity vectors and streamlines illustrate the flow direction.

Table 6. Mixing time uncertainty estimate on the medium (43,956 cells) mesh (GCI^{32}). reported for all tracer injection points.

Tracer	GCI^{32} [%]
1	10
2	3
3	3
4	13
5	12
6	0.8
7	0.8
8	10
9	7
Average	7

3.1. Theoretical Model Cases

Figure 9 and Table 7 present the mixing time differences between using the effective diffusion coefficient and using only the laminar diffusion coefficient. This generally has a large impact on mixing time. Similar to the water model simulations, there are variations in mixing times depending on the location of the tracer injection. However, when the turbulent diffusion contribution to mixing is removed, the convective contribution still has a large impact at Points 5 and 9. At these points, the mixing time only increases approximately 20 s (270%) compared to the maximum which increases approximately 170 s (1000%). Since Point 9 is in the plume, it will likely be the most representative mixing time, as the plume is the reaction zone, hence, the region of change in the process. This is important to remember when comparing test a to b.

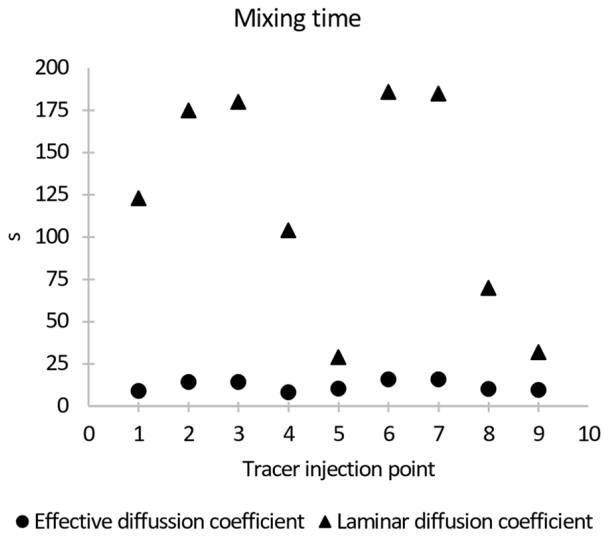

Figure 9. Mixing times for different tracer injections with varying diffusion coefficients.

Table 7. Mixing time differences in the metal reactor with effective diffusion coefficient and (only) the laminar diffusion coefficient.

Tracer	Effective Diffusion (s)	Laminar Diffusion (s)	Δ_{mix} (s)
1	9	123	114
2	14.4	175	160
3	14.4	180	165
4	8.3	104	96
5	10.4	29	19
6	15.9	186	170
7	15.9	185	169
8	10.2	70	60
9	9.6	32	22
Average	12 ± 3	120 ± 61	

3.1.1. Comparison of Cases 1–4a

Table 8 presents the total simulation time for each case setup when the reactions were included. The choice of core configuration for each case was determined by the need to balance multiple simulations while optimizing computational resources. Given the computational intensity of the simulations, distributing the available cores across multiple cases allowed for more tests within a reasonable time frame. Among the cases considered, Cases 1, 3, and 4 involve calculations for an equal number of cells. However, there are distinct variations in their reaction mechanisms, notably, Case 1 triggers reactions only every six timesteps, while both Case 3 and Case 4 triggers reactions at every timestep. Consequently, one can anticipate an increase in simulation time for Cases 3 and 4 when restricted to eight computing cores. While Case 2, like Cases 3 and 4, initiates reactions at each timestep, its simulation time requirement remains comparatively shorter. This discrepancy can be attributed to the reduced number of cells that partake in reactions during each individual timestep. As the core count increases, the simulation time decreases, with the main limitation being the number of cells partaking in chemical reactions.

Table 8. The simulation time for calculations including chemical reactions for 600 s.

Case	Time (h)	Cores
1	22	8
2	6	8
3	20	16
4	20	16

A comparative analysis of Case 1a through Case 4a, encompassing their respective reactions, is depicted in Figure 10, wherein the mass of all elements and the mean temperature across the domain are displayed. The results demonstrate noticeable differences among the cases. The initial observation, as depicted in Figure 10a, reveals a diminished decarburization rate in Case 2a as compared with the other cases. This difference can be attributed to the increased pressure at which all reactions occur, since all reactions only occur in the jet region. It is also seen that Case 1a exhibits the highest initial rate of decarburization, which should be due to the distribution of oxygen across the entire gas plume that, in turn, permits a lower pressure equilibrium for a larger portion of the reactions. The difference when comparing Case 1a to Cases 3a and 4a is not large, indicating that the simplification in Case 1a could be used for the current state of the process. Cases 3a and 4a are quite similar, indicating that the turbulence mixing limitation on the reactions does not pose a significant difference compared to perfect mixing in the cells, when it comes to decarburization reactions within the current composition range. Figure 10b,c show the iron and oxygen content in the melt. A decrease in iron content indicates that formation of solid oxides has occurred, while an increase in oxygen indicates that liquid oxides have formed and/or that the dissolved oxygen content in the melt has increased. It is seen that Case 2a leads to an earlier formation of liquid and solid oxides compared to the other cases. However, at the end of the simulation, the differences in iron content are very small between Cases 2a and 1a, and small between Cases 2a and 3a. Only Case 4a exhibits significantly lower iron losses at the end of the simulation. When observing the oxygen content at the end of the simulation, it is also seen that the differences are small among Cases 1–3a, and Case 4a has a lower oxygen content in the melt. The temperature, Figure 10d, follows the decarburization and oxide formation found in Figure 10a–c. It can be concluded that the turbulence-limited reactions of Case 4a lead to less solid and liquid iron oxide formation, while maintaining a similar carbon content as Cases 1a and 3a at the end of the simulation. Forcing all reactions to only occur at the injection zone (Case 2a) leads to the worst rate of decarburization and the highest iron losses. The differences are relatively small, though and the largest impact can be seen in the temperature evolution of the various cases.

In Cases 1a to 3a, where the equilibrium fraction η^{eq} is set to unity for all cells, regardless of turbulence, the supplied oxygen within the cell is completely consumed during the equilibrium reaction. However, except for Case 2a, all cases enable reactions to occur throughout the entire plume, considering a pressure variance of approximately 30,000 Pa. This pressure difference has implications for the decarburization process, primarily because of the lower partial pressure of CO gas in proximity to the surface. In Case 1a, the injected oxygen is evenly distributed throughout the reaction zone. In contrast, Case 3a and Case 4a include the transport of reacted gas from the inlet to the surface of the bath. Consequently, Case 1a will facilitate a greater amount of oxygen to react at a lower partial pressure of CO, which explains the higher decarburization rate. While the carbon content decreases to lower levels, oxygen is utilized in the formation of iron oxide. However, even as the decarburization rate diminishes, there is still ongoing carbon oxidation near the upper region of the bath. This constitutes the primary distinction between Case 2a and the remaining cases, as illustrated in Figure 11, where a carbon concentration snapshot can be seen at the end of the simulation (equilibrium state at the end of a timestep). The pressure in the reaction zone clearly has an effect, which is to be expected. The impact of the turbulence limited reactions is evident in all graphs presented in Figure 10, particularly

when comparing Case 3a and Case 4a. It is observed that the decarburization rate in Case 4a is lower compared to Case 3a, while the formation of iron oxide occurs earlier (at around 250 s) and at a higher rate than in Case 4a (at around 280 s). Consequently, this leads to a reduced temperature evolution in Case 4a. These observations are in line with expectations, considering that the equilibrium fraction η^{eq}, due to turbulence, is set to unity for all cells in Case 3a, while it varies in Case 4a, as shown in Figure 12. Note that the difference between Cases 3a and 4a is not particularly large, which is easily explained since the equilibrium fraction is close to or higher than one in a majority of the gas plume. The lower part of the plume has a region where the equilibrium fraction is lower than one, which means that the reactions taking place at the highest ferro-static pressure do not have time to fully reach equilibrium within one timestep. This influences the formation of solid oxides and the temperature, as was described previously.

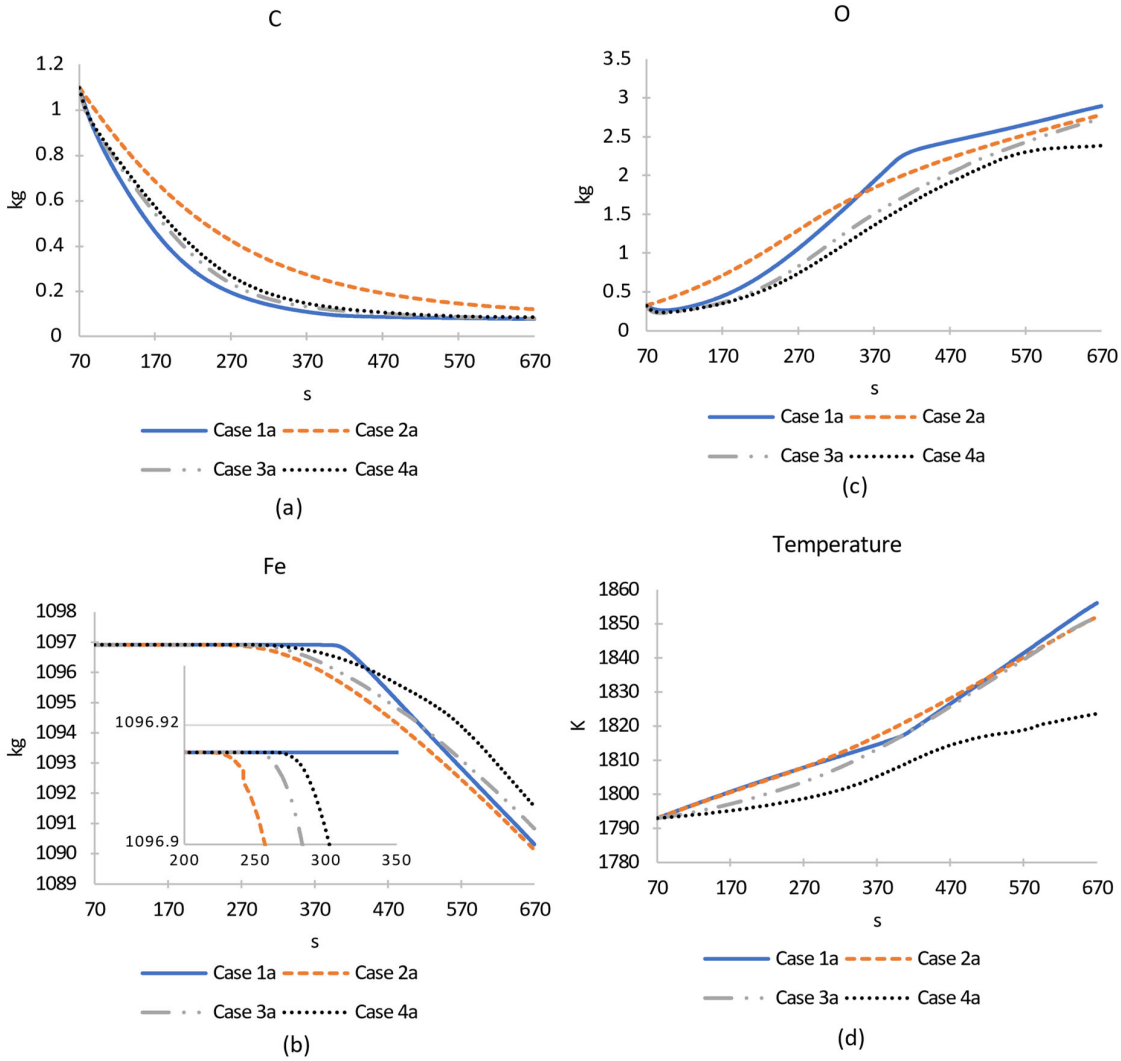

Figure 10. The graphs show the element and temperature evolution in the domain over time: (**a**) Carbon mass; (**b**) iron mass; (**c**) oxygen mass; (**d**) temperature.

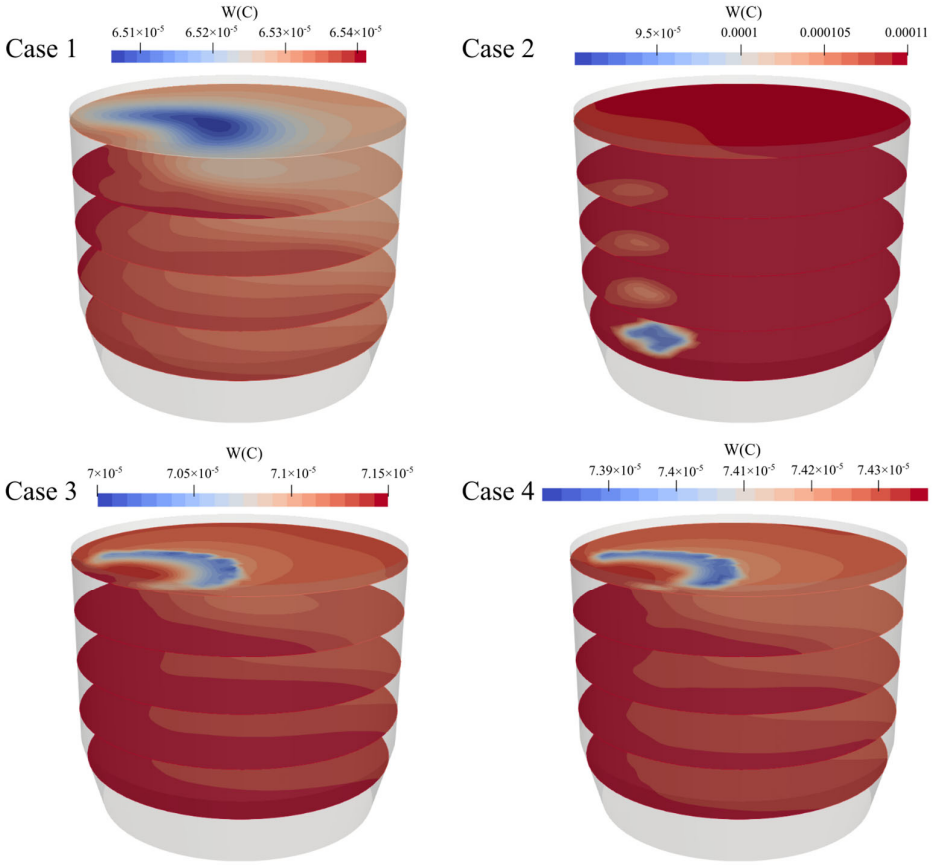

Figure 11. Iso-planes display the carbon content at the end of the simulation (660 s) in Cases 1a–4a. Note, there is no carbon oxidation in the above region of Case 2a, the gradient in the upper iso-planes is the effect of the flow spreading the reacted melt.

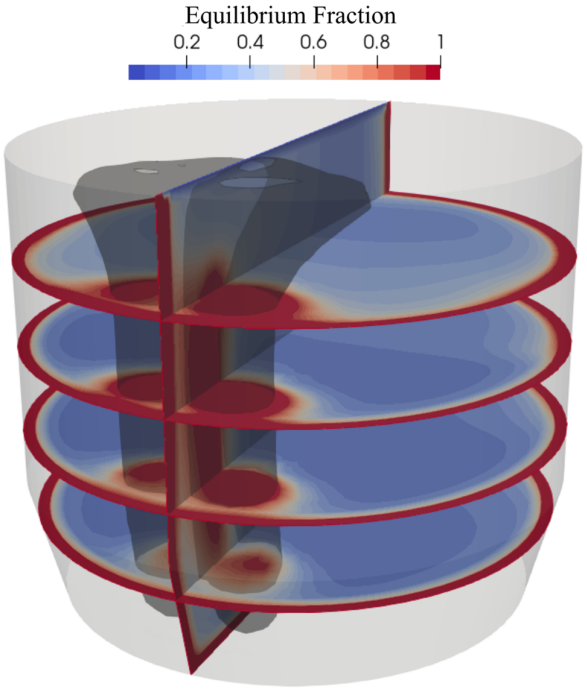

Figure 12. Iso-planes display the equilibrium fraction due to turbulence mixing in the cells for Case 4. The transparent black volume (plume shape) illustrates the reaction zone. Note that values higher than one are displayed as 1.

3.1.2. Test 2, Mixing Time Effect on Reactions in Cases 1–4

Figure 13 presents the mass of carbon and iron in Cases 1a, 2a, and 4a (including turbulent diffusion of mass) and Cases 1b, 2b, and 4b (only laminar diffusion of mass). It is seen that the increase in mixing time caused by removing turbulent diffusion does not affect the composition throughout the process, both for carbon (Figure 13a) and iron (Figure 13b). The removal of turbulent diffusion is an artificial way of increasing the mixing time, to observe the effects of such an increase without changing the gas flow rate in the system. As stated above, the reaction zone is the source of change in the process wherein the mixing time only increases approximately 20 s, when turbulent diffusion of mass is neglected (see Table 7). It should be noted that the mixing time increases by more than 270%. However, this increase only corresponds to about 4% of the total process time, which may be the reason for the low impact it has on the end results. Therefore, the current process is mainly limited by thermodynamics and the rate of gas injection. In other process stages (e.g., later decarburizing stages in an AOD), it is possible that a corresponding increase in mixing time might affect the end state. It is also likely that less intensely stirred systems such as ladles might experience a completely different response. In Figure 14, the local changes of carbon content over 7 s are displayed for Cases 4a, and 4b. The figure shows that the transport of the reacted melt across the domain is faster when turbulent diffusion is considered, providing local variations between the cases. However, as seen in Figure 15, the local variations seen in Figure 14 do not affect the carbon content as much. Naturally, the maximum/minimum values of Case 4b (with only laminar mass diffusion) is higher/lower compared to Case 4a where the higher mass diffusion leads to smoother gradients. Overall, the results, once again, point to a system that is governed by thermodynamics and the supply of oxygen rather than the mixing in the process. So, while an increase in mixing time of 270% might sound detrimental to the process, it is not certain that it will negatively affect the process. To put it in other words, investigations that only focus on mixing time may miss the target since it cannot be concluded that a lower mixing time is always beneficial to the process.

3.1.3. Test 3, Initial Oxygen Effect in Cases 1–4

The carbon mass is compared between Cases 1–4a and Cases 1–4c, wherein the initial oxygen content is decreased, as outlined in Table 5. Initial oxygen levels in the melt are seldom part of the sampling done at steel plants. The dissolved oxygen content in the melt may, or may not, be at an equilibrium state at the start of the process. This analysis looks at the effects of a variation in the initial oxygen content in the melt. Figure 16 reveals that the oxygen content in the melt plays a significant role in decarburization. Cases 1a, 3a, and 4a all show an increased rate of decarburization for the first 300 s compared to the lower initial oxygen content in the melt of Cases 1c, 3c, and 4c. Cases 2a and 2c do not show this trend. This distinction can be attributed to the reactions taking place in the plume, as the oxygen in the melt reacts with the ascending gas. Notably, there is a more pronounced difference observed in Case 3 and Case 4 compared to Case 1. This discrepancy arises from the fact that the injected oxygen primarily reacts at the inlet, resulting in the gas plume consisting mostly of CO in Case 3 and Case 4. Consequently, the oxygen in the melt contributes to a higher oxygen content within each cell and exerts a more significant influence on the reactions, since there will be more oxygen available higher up in the plume. Conversely, in Case 1, the injected oxygen is already distributed throughout the plume, thereby diminishing the contribution of the initial dissolved oxygen in the melt to the reactions. The cases all tend towards the same decarburization rate with increasing time as the effect of the initial oxygen content wears off. Regardless, it is important to note that measuring the oxygen content of the melt can be important to accurately predict the initial stage of decarburization. The different behavior in Case 2 can be described by the limited reaction zone that is only close to the nozzles, i.e., no additionally available oxygen at lower ferro-static pressure as in the other cases. Also, when considering Figure 10b,c, it is understood that Case 2a almost immediately forms liquid iron oxides. At a lower initial

oxygen content, there will be less liquid iron oxide formation, while approximately the same amount of oxygen is participating in the decarburization reactions, as can also be seen in Case 4 in Figure 17.

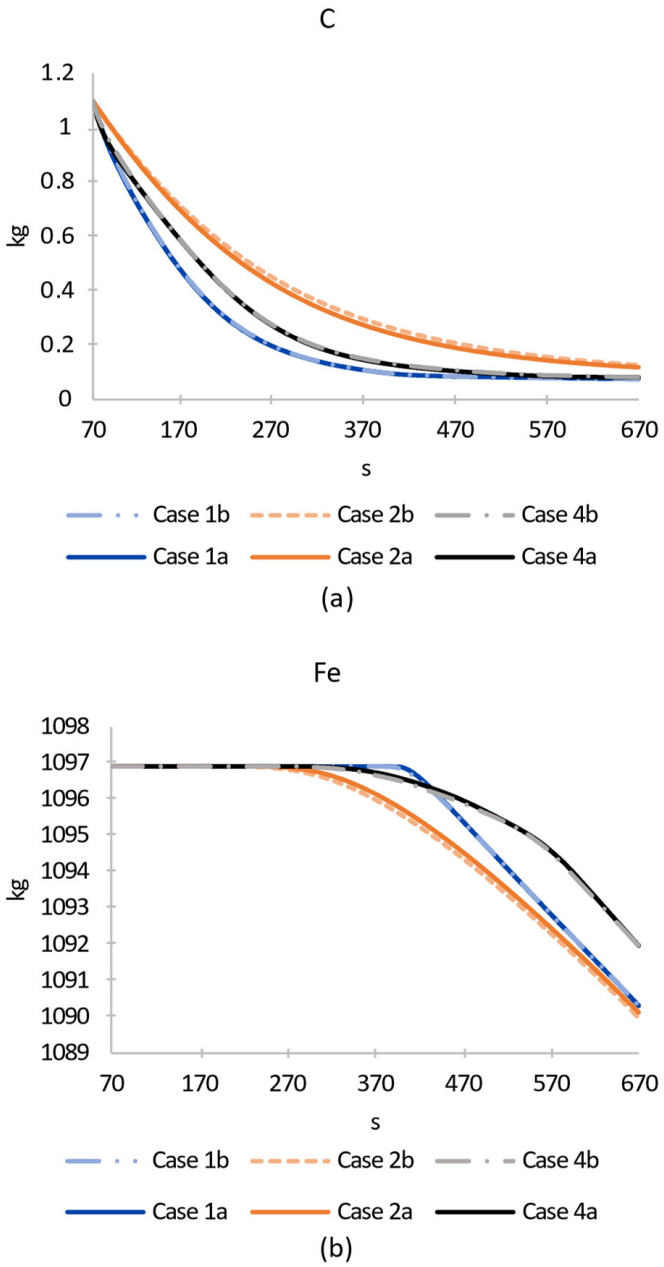

Figure 13. The element mass in the domain over time using effective diffusion (Cases 1a, 2a, and 4a) as well as only laminar diffusion (Cases 1b, 2b, and 4b): (**a**) Carbon mass; (**b**) iron mass.

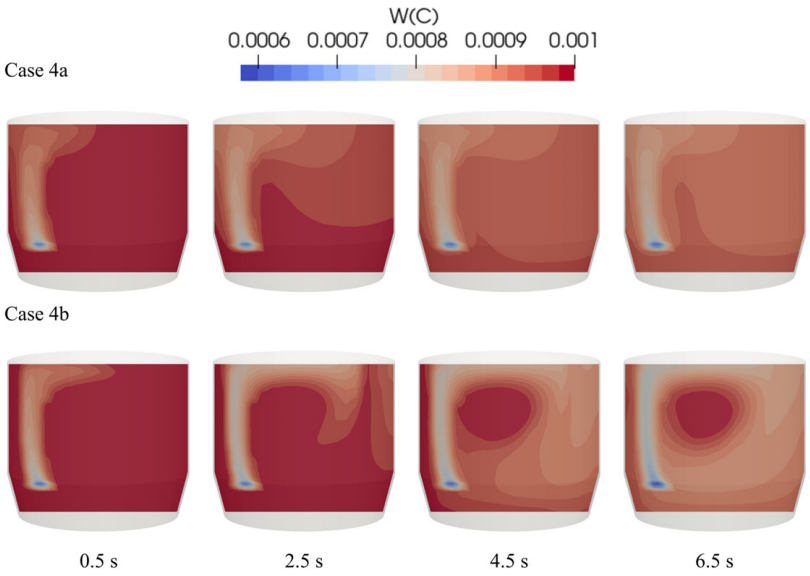

Figure 14. Four time frames between 0 and 7 s, showing the local changes of carbon content in Case 4a (effective diffusion) and 4b (laminar diffusion only).

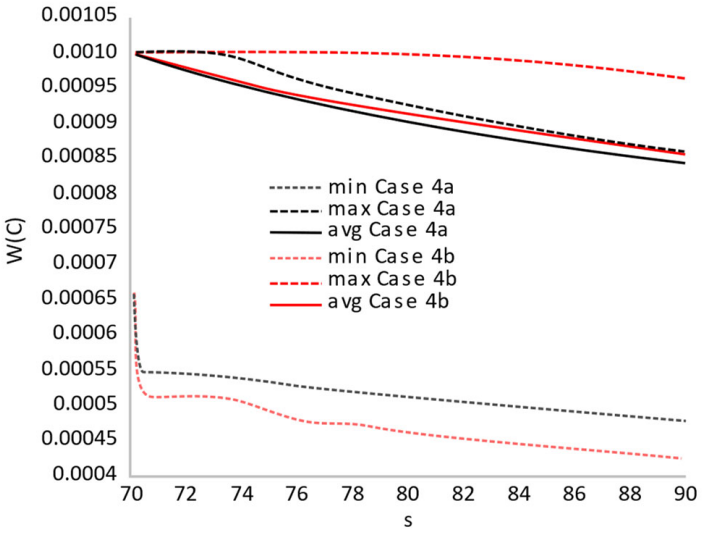

Figure 15. Compares the maximum, average, and minimum carbon content in the melt over 20 s for Cases 4a (including turbulent diffusion) and 4b (laminar diffusion only).

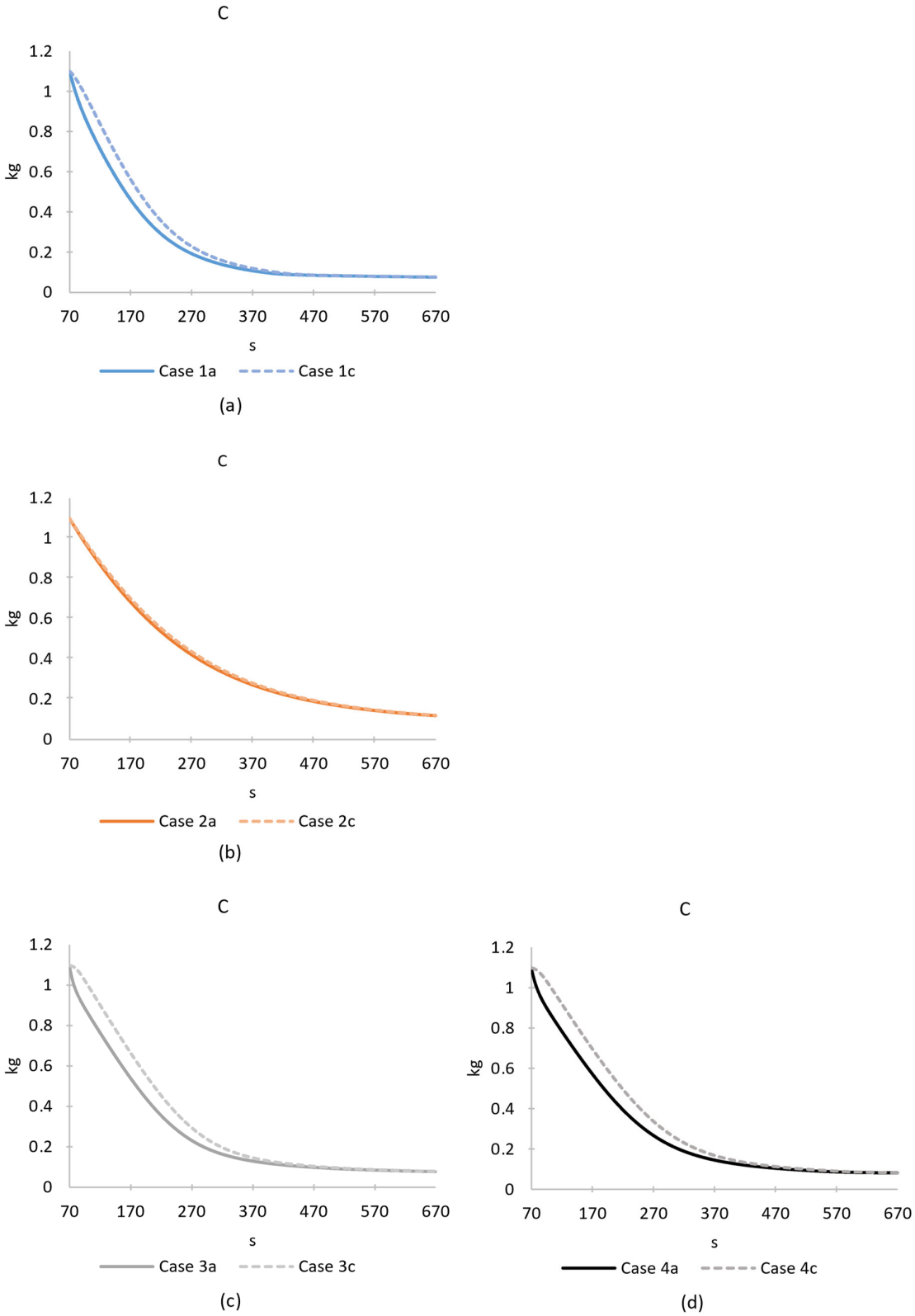

Figure 16. The graphs show the mass of carbon in the domain over time for Cases 1–4 between Test a (higher initial oxygen content) and Test c: (**a**) Case 1; (**b**) Case 2; (**c**) Case 3; (**d**) Case 4.

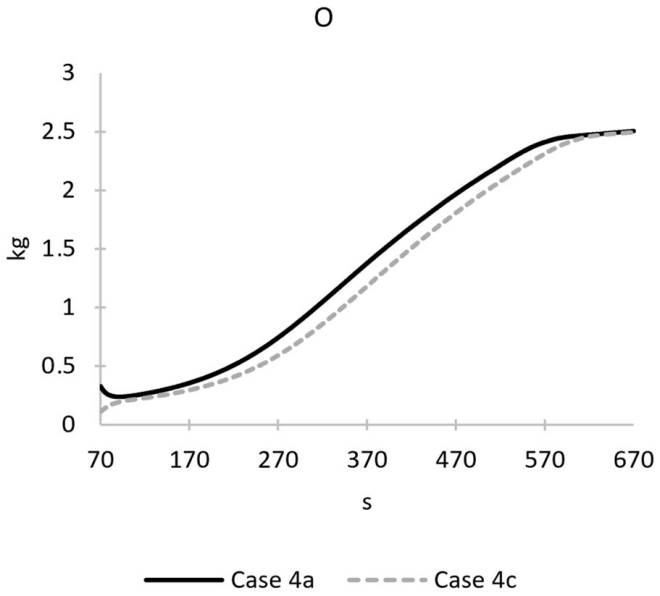

Figure 17. The graphs show the mass of oxygen in the domain over time for Case 4 between Test a (higher initial oxygen content) and Test c.

At the current state, the model provides a practical approach to coupling between CFD and chemical reactions by sacrificing some accuracy in the flow and energy transport calculations. While this provided the possibility to investigate the impact of mixing time on the decarburization and added transparency to the system, further work is needed to better represent the complexity in the dynamics and mixing of such intensely stirred processes, e.g., including a free surface and applying a finer mesh. In addition, the reaction between metal and slag as well as the mass transport of solid slags needs to be investigated to judge if it is necessary to resolve those phases for more accurate description of industrial cases. For instance, chromium oxidation is unwanted in the AOD converter which is partially prevented by lowering the partial pressure of the CO gas to force decarburization instead. However, as seen in this work, at a lower pressure, oxidation of elements in the liquid such as iron is feasible. Thus, in an industrial AOD where the pressure is even higher at the injection zone, chromium will also oxidize. As these oxides are driven upwards to lower pressure regions, they continuously react with the gas and melt. This complex phenomenon can only be thoroughly studied when the model includes the transport of solid slag and the reactions between solid slag and melt. Cases 3 and 4, in particular, are interesting candidates for these model developments as they are expected to provide better insight into what happens if reaction kinetics in the plume has a larger influence on other process steps. Since the current model already utilizes parallel decomposition of the domain, an increase in resolution is possible and a straightforward next step. The other developments remain as opportunities for further studies.

4. Conclusions

A practical model that was capable of simulating fluid dynamics with chemical reactions in a side-blowing metallurgical reactor was developed to specifically study the effect of mixing time on decarburization. The model employed cell-local equilibrium with a turbulence limiter, while mass, momentum, and energy transfer were calculated using a finite volume method CFD approach. The mixing time and flow structure of the bath were validated against a water model, and then different reaction methods were investigated. Overall, the findings show the interplay between mixing, pressure, oxygen distribution, and turbulence in the decarburization process.

Specifically:

The location of the tracer injection is important when determining mixing time. Injection points located in the rising plume or in regions where the bath is affected by strong currents clearly showed a faster mixing of the tracer. Since reactions occur at the interface of the gas plume, it is recommended to use tracer injection in this region in all systems where reactions originate from this interaction, in order to get a representative mixing time.

The highest initial decarburization rate was found in the case where oxygen was distributed across the gas plume, which fostered a lower equilibrium pressure for reactions. The least favorable decarburization rate and the highest iron losses were exhibited in the case where all reactions were assumed to occur solely in the injection zone. A turbulence limiter for the reaction rate was also introduced which influenced decarburization, solid oxide formation, and temperature evolution.

The mixing time was artificially manipulated in one case by removing the turbulent mass diffusion contribution, leading to an increased mixing time. Surprisingly, this had minimal influence on the carbon and iron compositions throughout the process. Despite an increase in mixing time of approximately 270%, it was clear that the dominant drivers of this system are thermodynamics and gas injection rates. The current process's complexity is shaped more by thermodynamics and oxygen supply than by mixing time. To put it in other words, investigations that only focus on the mixing time may miss the target, since it cannot be concluded that a lower mixing time is always beneficial to the reactive process.

Author Contributions: Conceptualization, S.C. and M.E.; methodology, S.C. and M.E.; software, S.C., H.L. and M.E.; validation, S.C., H.L. and M.E.; formal analysis, S.C.; investigation, S.C.; resources, M.E.; data curation, S.C.; writing—original draft preparation, S.C.; writing—review and editing, H.L. and M.E.; visualization, S.C.; supervision, H.L. and M.E.; project administration, M.E.; funding acquisition, M.E. All authors have read and agreed to the published version of the manuscript.

Funding: This research has received funding from Vinnova under grant agreement number: 2018-02386.

Data Availability Statement: The data presented in this study are available on request from the corresponding author. The data are not publicly available due to privacy.

Acknowledgments: The authors wish to express gratitude to the Jernkontoret (Swedish steel producers association) committee and project 23033 (VARIAOD2) members, along with the Metalliska Material program, for their contributions by insightful discussions and valuable industrial perspectives. A heartfelt acknowledgment is also extended to VINNOVA, The Swedish Innovation Agency, for their financial backing. Our deepest thanks for your support and role in facilitating this research.

Conflicts of Interest: The authors declare no conflict of interest.

Nomenclature

α	Volume fraction	[-]
$\vec{v}$	Velocity vector	[m·s^{-1}]
ρ	Density	[kg·m^{-3}]
$\dot{m}_{pq}$	Mass transfer between phases	[kg·s^{-1}·m^{-3}]
p	Pressure	[Pa]
$\vec{g}$	Gravitational acceleration	[m·s^{-2}]
K_{pq}	Momentum exchange coefficient	[kg·m^{-2}·s^{-1}]
μ_{eff}	Effective viscosity	[kg·m^{-1}·s^{-1}]
τ_p	Particulate relaxation time	[s]
d_b	Bubble diameter	[m]
A_i	Interfacial area	[m^2]
C_D	Drag coefficient	[-]
Re	Reynolds number	[-]
μ	Molecular viscosity	[kg·m^{-1}·s^{-1}]
μ_t	Turbulent viscosity	[kg·m^{-1}·s^{-1}]
k	Turbulent kinetic energy	[m^2·s^{-2}]

ε	Turbulent dissipation rate	$[m^2 \cdot s^{-3}]$
σ_k	Turbulent Prandtl number for k	[-]
σ_ε	Turbulent Prandtl number for ε	[-]
ν	Kinematic viscosity	$[m^2 \cdot s^{-1}]$
h	Specific enthalpy	$[J \cdot kg^{-1}]$
k_{eff}	Effective thermal conductivity	$[W \cdot m^{-1} \cdot K^{-1}]$
$\overline{\overline{\tau}}_{eff}$	Shear energy	[J]
e	Specific energy	$[J \cdot kg^{-1}]$
$\dot{m}$	Mass flow rate	$[kg \cdot s^{-1}]$
V	Volume	$[m^3]$
$\varnothing_q^i$	Scalar in phase q	[-]
Γ	Diffusion coefficient	$[kg \cdot m^{-1} s^{-1}]$
D_m	Molecular mass diffusivity	$[m^2 \cdot s^{-1}]$
D_t	Turbulent diffusivity	$[m^2 \cdot s^{-1}]$
SC_t	Turbulent Schmidt number (0.7)	[-]
$\xi^{*\prime}$	Volume fraction occupied by fine structures	[-]
C_ξ	Volume fraction constant	[-]
τ^*	Reaction time scale in fine structures	[s]
C_τ	Time scale constant	[-]
η^{eq}	Equilibrium fraction	[-]
t_s	Timestep	[s]

References

1. Ersson, M.; Tilliander, A. Review on CFD Simulation and Modeling of Decarburization Processes. *Steel Res. Int.* **2018**, *89*, 1700108. [CrossRef]
2. Zhu, M.Y.; Sawada, I.; Iguchi, M. Physical Characteristics of a Horizontally Injected Gas Jet and Turbulent Flow in Metallurgical Vessels. *ISIJ Int.* **1998**, *38*, 411–420. [CrossRef]
3. Odenthal, H.J.; Thiedemann, U.; Falkenreck, U.; Schlueter, J. Simulation of Fluid Flow and Oscillation of the Argon Oxygen Decarburization (AOD) Process. *Metall. Mater. Trans. B* **2010**, *41*, 396–413. [CrossRef]
4. Wuppermann, C.; Giesselmann, N.; Rückert, A.; Pfeifer, H.; Odenthal, H.J.; Hovestädt, E. A Novel Approach to Determine the Mixing Time in a Water Model of an AOD Converter. *ISIJ Int.* **2012**, *52*, 1817–1823. [CrossRef]
5. Wuppermann, C.; Rückert, A.; Pfeifer, H.; Odenthal, H.J. Physical and Mathematical Modeling of the Vessel Oscillation in the AOD Process. *ISIJ Int.* **2013**, *53*, 441–449. [CrossRef]
6. Tilliander, A.; Jonsson, T.L.I.; Jönsson, P. A Three-Dimensional Three-Phase Model of Gas Injection in AOD Converters. *Steel Res. Int.* **2014**, *84*, 1300065. [CrossRef]
7. Visuri, V.; Ishookana, E.; Kärna, A.; Haas, T.; Erie, R.H.; Fabritius, T. A Physical modelling study of mixing in an AOD vessel. In Proceedings of the 5th International Conference on Process Development in Iron and Steelmaking, Luleå, Sweden, 12–15 June 2016.
8. Wimmer, W.; Kahrimanovic, D.; Pastucha, K.; Voraberger, B.; Wimmer, G. Computational Fluid Dynamics Simulations for Understanding and Optimizing the AOD Converter. *Huettenmaenn Monatsh* **2020**, *165*, 3–10. [CrossRef]
9. Cheng, Z.; Wang, Y.; Dutta, A.; Blanpain, B.; Guo, M.; Malfiet, A. Numerical Study of Fluid Flow and Mixing in the Argon Oxygen Decarburization (AOD) Process. *ISIJ Int.* **2023**, *63*, 492–503. [CrossRef]
10. Wei, J.H.; Zhu, D.P. Mathematical modeling of the argon-oxygen decarburization refining process of stainless steel: Part I. Mathematical model of the process. *Metall. Mater. Trans. B* **2002**, *33*, 111–119. [CrossRef]
11. Wei, J.H.; Zhu, D.P. Mathematical modeling of the argon-oxygen decarburization refining process of stainless steel: Part II. Application of the model to industrial practice. *Metall. Mater. Trans. B* **2002**, *33*, 121–127. [CrossRef]
12. Zhu, H.L.; Wei, J.H.; Shi, G.M.; Shu, J.H.; Jiang, Q.Y.; Chi, H.B. Preliminary Investigation of Mathematical Modeling of Stainless Steelmaking in an AOD Converter: Mathematical Model of the Process. *Steel Res. Int.* **2007**, *78*, 305–310. [CrossRef]
13. Shi, G.M.; Wei, J.H.; Zhu, H.L.; Shu, J.H. Preliminary Investigation of Mathematical Modeling of Stainless Steelmaking in an AOD Converter: Application of the Model and Results. *Steel Res. Int.* **2007**, *78*, 311–317. [CrossRef]
14. Wei, J.H.; Cao, Y.; Zhu, H.L.; Chi, H.B. Mathematical Modeling Study on Combined Side and Top Blowing AOD Refining Process of Stainless Steel. *ISIJ Int.* **2011**, *51*, 365–374. [CrossRef]
15. Ersson, M.; Höglund, L.; Tilliander, A.; Jonsson, T.L. Dynamic Coupling of Computational Fluid Dynamics and Thermodynamics Software: Applied on a Top Blown Converter. *ISIJ Int.* **2008**, *48*, 147–153. [CrossRef]
16. Järvinen, M.; Kärna, A.; Fabritius, T. A Detailed Single Bubble Reaction Sub-Model for AOD Process. *Steel Res. Int.* **2010**, *80*, 429–436.
17. Järvinen, M.; Pisilä, S.; Kärna, A.; Ikähemonen, T.; Kupari, P.; Fabritius, T. Fundamental Mathematical Model for AOD Process. Part I: Derivation of the Model. *Steel Res. Int.* **2011**, *82*, 638–649. [CrossRef]

18. Pisilä, S.; Järvinen, M.; Kärnä, A.; Ikäheimonen, T.; Fabritius, T.; Kupari, P. Fundamental Mathematical Model for AOD Process. Part II: Model validation. *Steel Res. Int.* **2011**, *82*, 1000266. [CrossRef]
19. Järvinen, M.; Visury, V.V.; Heikkinen, E.P.; Kärna, A.; Sulasami, P.; De Blasio, C.; Fabritius, T. Law of Mass Action Based Kinetic Approach for the Modelling of Parallel Mass Transfer Limited Reactions: Application to Metallurgical Systems. *ISIJ Int.* **2016**, *56*, 1543–1552. [CrossRef]
20. Van Ende, M.A.; Kim, Y.M.; Cho, M.K.; Choi, J.; Jung, I.H. A Kinetic Model for the Ruhrstahl Heraeus (RH) Degassing Process. *Metall. Mater. Trans. B* **2011**, *42*, 477–489. [CrossRef]
21. Andersson, N.; Tilliander, A.; Jonsson, L.T.T.; Jönsson, P. Fundamental decarburisation model of AOD process. *Ironmak. Steelmak.* **2013**, *40*, 390–397. [CrossRef]
22. Andersson, N.; Tilliander, A.; Jonsson, L.T.T.; Jönsson, P. An in-Depth Model-Based Analysis of Decarburization in the AOD Process. *Steel Res. Int.* **2012**, *83*, 1039–1052. [CrossRef]
23. Van Ende, M.A.; Jung, I.H. A Kinetic Ladle Furnace Process Simulation Model: Effective Equilibrium Reaction Zone Model Using FactSage Macro Processing. *Metall. Mater. Trans. B* **2017**, *48*, 28–36. [CrossRef]
24. Mason, P.; Grundy, A.N.; Retting, R.; Kjellqvist, L.; Jeppson, J.; Bratberg, J. The Application of an Effective Equilibrium Reaction Zone Model Based on CALPHAD Thermodynamics to Steel Making. In Proceedings of the 11th International Symposium on High-Temperature Metallurgical Processing, San Diego, CA, USA, 23–27 February 2020; pp. 101–113.
25. Wei, W.J.; Gustavsson, J.; Samuelsson, P.; Gyllenram, R.; Tilliander, A.; Jönsson, P.G. Prediction of nitrogen behaviour in the AOD process by a time-dependent thermodynamic model. *Ironmak. Steelmak.* **2022**, *49*, 70–82. [CrossRef]
26. Chanouian, S.; Ahlin, B.; Tilliander, A.; Ersson, M. Inclination Effect on Mixing Time in a Gas–Stirred Side–Blown Converter. *Steel Res. Int.* **2021**, *92*, 2100044. [CrossRef]
27. Chanouian, S.; Ahlin, B.; Tilliander, A.; Ersson, M. A Fundamental Investigation of Decarburization Reactions in the Argon–Oxygen Decarburization Converter Using Coupled Computational Fluid Dynamics and Thermodynamics Databases. *Steel Res. Int.* **2022**, *93*, 21000156. [CrossRef]
28. Haas, T.; Schubert, C.; Eickhoff, M.; Herbert, P. Numerical Modeling of the Ladle Flow by a LES-Based Eulerian–Lagrange Approach: A Systematic Survey *Met. Mater. Trans. B* **2021**, *52*, 903–921. [CrossRef]
29. Haas, T.; Schubert, C.; Eickhoff, M.; Herbert, P. Full-Scale Large Eddy Simulation of a 185 t Ladle Optimizing a Hybrid Eulerian Grid and a Discrete Bubble Mapping Approach. *Steel Res. Int.* **2021**, *93*, 100653. [CrossRef]
30. ANSYS FLUENT: User's Guide, ANSYS FLUENT, Version R2. 2022. Available online: https://www.ansys.com/ (accessed on 27 August 2023).
31. Schiller, L.; Naumann, Z.L. A Drag Coefficient Correlation. *Ver. Deutsch. Ing.* **1935**, *77*, 318.
32. Shin, T.H.; Liou, W.W.; Shabbir, A.; Yang, Z.; Zhu, J. A New $k-\varepsilon$ Eddy-Viscosity Model for High Reynolds Number Turbulent Flows—Model Development and Validation. *Comput. Fluids* **1995**, *24*, 227–238.
33. Andersson, J.O.; Helander, T.; Höglund, L.; Shi, P.F.; Sundman, B. Thermo-Calc and DICTRA, Computational tools for materials science. *Calphad* **2002**, *26*, 273–312. [CrossRef]
34. Thermo-Calc Software TCOX Metal Oxides Solutions Database Version 10. 2020. Available online: https://thermocalc.com/products/databases/metal-oxide-solutions/ (accessed on 23 February 2023).
35. Stremler, M. Mixing Measures. In *Encyclopedia of Microfluidics and Nanofluidics*; Li, D., Ed.; Springer: Boston, MA, USA, 2008; pp. 1376–1382.
36. Magnussen, B.F. On the Structure of Turbulence and a Generalized Eddy Dissipation Concept for Chemical Reaction in Turbulent Flow. In Proceedings of the 19th AIAA Meeting, St. Louis, MO, USA, 12–15 January 1981.
37. Celik, I.; Ghia, U.; Roache, P.J.; Freitas, C.; Coloman, H.; Raad, P. Procedure for Estimation and Reporting of Uncertainty Due to Discretization in CFD Applications. *ASME J. Fluids Eng.* **2008**, *130*, 078001.